This is a repository copy of *Influence of additives on the in situ crystallization dynamics of methyl ammonium lead halide perovskites*.

Article

Influence of Additives on the *In Situ* Crystallization Dynamics of Methyl Ammonium Lead Halide Perovskites

Edwin Pineda De La O,* Noura Alhazmi, Stephen J. Ebbens, and Alan D. F. Dunbar

Read Online

ACCESS | Metrics & More | Article Recommendations | SI Supporting Information

ABSTRACT: Understanding the kinetics of the crystallization process for organometal halide perovskite formation is critical in determining the crystalline, nanoscale morphology and therefore the electronic properties of the films produced during thin film formation from solution. In this work, *in situ* grazing incidence small-angle X-ray scattering (GISAXS) and optical microscopy measurements are used to investigate the processes of nucleation and growth of pristine mixed halide perovskite (MAPbI$_{3-x}$Cl$_x$) crystalline films deposited by bar coating at 60 °C, with and without additives in the solution. A small amount of 1,8-diiodooctane (DIO) and hydriodic acid (HI) added to MAPbI$_{3-x}$Cl$_x$ is shown to increase the numbers of nucleation centers promoting heterogeneous nucleation and accelerate and modify the size of nuclei during nucleation and growth. A generalized formation mechanism is derived from the overlapping parameters obtained from real-time GISAXS and optical microscopy, which revealed that during nucleation, perovskite precursors cluster before becoming the nuclei that function as elemental units for subsequent formation of perovskite crystals. Additive-free MAPbI$_{3-x}$Cl$_x$ follows reaction-controlled growth, in contrast with when DIO and HI are present, and it is highly possible that the growth then follows a hindered diffusion-controlled mechanism. These results provide important details of the crystallization mechanisms occurring and will help to develop greater control over perovskite films produced.

KEYWORDS: perovskite, small-angle X-ray scattering, optical microscopy, crystallization, bar coating, dynamics
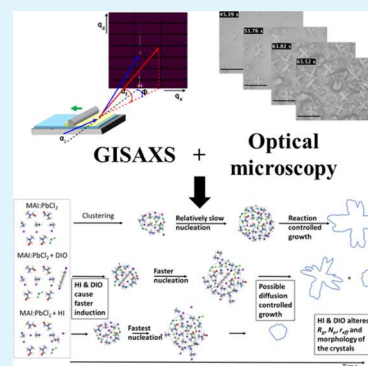
1. INTRODUCTION

Since their first reported efficiency of 3.8% in 2009, perovskite solar cells have rapidly reached a record efficiency of 25.2% in 2019.[1] A lot of effort has been put into developing and controlling deposition to fulfill their potential to offer devices at low cost, with easy fabrication, and high efficiency. Protocols such as thermal annealing,[2−5] using additives,[6−10] modifying the concentration used,[11,12] applying antisolvents, using different solvents,[3,13] and high-temperature casting[14] have all been investigated to control perovskite structure, grain size, crystallinity, surface coverage, and stability with varying success. There is a large volume of published research describing successful protocols to improve perovskite solar cell efficiencies.[15−17] To fully understand the effects caused by these different treatments, it is necessary to consider how they control the nucleation and growth and therefore manipulate the size, purity, morphology, and crystal structure, such that it is possible to create reproducible perovskite thin films with the desired physical and morphological properties. To date, the phenomenon of perovskite crystallization is not well understood, largely because the main research focus has been on the production and improvement of highly efficient solar cells. There are also some challenges in studying crystallization, such as the difficulty in measuring the critical nucleus sizes in the range of 100−1000 atoms,[18] a real challenge for current experimental methods. Microscopic techniques can detect and observe relatively small

sizes but these techniques do not distinguish the crystal structure.[19] Observation of early crystal growth on the lattice scale is only possible in real-time during the rapidly drying liquid phase, making these observations very challenging. Several different approaches have been employed to observe the thermodynamics and kinetics of nucleation and crystal growth, e.g., atomic force microscopy (AFM), scanning electron microscopy (SEM), X-ray diffraction (XRD), optical microscopy, interferometry, or differential scanning calorimetry (DSC).[18,20]

The phenomena of nucleation and growth from solution have been described by classic nucleation theory (CNT) and the Lifshitz−Slyozov−Wagner (LSW) growth model. In CNT, the solution precursor is deposited onto a substrate and the solvent is removed (mainly by heating), which causes supersaturation of the solution. The free energy of the system changes, and the atoms, ions, molecules, or other chemical species come together to form nuclei or embryos, which eventually act as a center of crystallization. Nuclei may form either in the solution or on a

substrate or any particle such as an additive and are referred to as homogeneous and heterogeneous nucleations, respectively.[19] If homogeneous nucleation is considered thermodynamically by examining the change in the free energy of a spherical particle, the total free energy ΔG is the sum of the surface free energy ΔG_s (free energy between a very large particle and the solute in the solution). The change in the free energy ΔG_r as a function of the nucleus radius r is given by

$$\Delta G_r = \Delta G_s + \Delta G_v = 4\pi r^2 \gamma - \frac{4}{3}\pi r^3 \Delta G_v \qquad (1)$$

where γ is the solid−liquid interfacial area free energy. The formation of a new nucleus depends on a cluster achieving the critical radius r^*, which is associated with the free-energy maxima barrier. If $r < r^*$, the system will dissolve the solid and further reduce its free energy because a small r is more stable, while when $r > r^*$, the solid will grow and the free energy will decrease, so the larger r is, the more stable the system becomes.[21,22] As stated in the LSW theory, the temporal rate of change in the nuclei size r follows a power law over time $r \propto t^x$. The exponent x can provide insight into the growth mechanism: if such an exponent is 1/2, the system experiences a dynamic coalescence (reaction-limited growth) and when it is 1/3 the growth is governed by Ostwald ripening (diffusion-limited growth).[23−25]

Spin casting is by far the most commonly used technique for the preparation of thin films of perovskite for solar cell applications. Much of the knowledge regarding film formation has been due to studying this technique. However, other deposition methods are better suited to transition from laboratory to large-scale production of perovskite, e.g., bar coating, blade coating, spray coating, or slot-die printing. Bar coating is a simple solution-based deposition technique for large areas with the added attraction of being industrially scalable. The system comprises a wire wound bar sitting in contact with a usually fixed substrate. The diameter of the wire and the spacing between windings determine the thickness of the wet films produced when the bar pushes the solution across the substrate. The bar coating process involves two major steps after spreading of the ink solution onto the substrate: (1) formation of a wet film and (2) drying of the wet film.[26] As the bar pushes the solution across the substrate, a small amount of solution passes through the gaps between the wire forming surface morphologies consisting of a series of strips, which collapse immediately due to superficial tension to result in a flat wet film.[27] The speed of the bar is crucial to form a wet film; if the speed is low, the deposition is under an evaporative regime, in contrast to that at higher print speeds under the Landau−Leviche mode where first there is formation of a wet film before solvent evaporation.[28,29]

Synchrotron radiation-based X-ray techniques allow structural characterization providing valuable information about the inner film morphology, e.g., wide-angle X-ray scattering (WAXS) probes length scales in the atomic range and thus yields crystallographic information about the sample,[30] while GISAXS is a technique that is surface-sensitive (due to the grazing incidence used) and probes longer length scales, thus providing a full mesoscale approach to the problem of crystallization and the morphology of the samples.[19,20] X-ray scattering at small angles (0.1−10°) allows information to be obtained regarding the structure in the range from 1 to 1000 nm. The use of fast two-dimensional (2D) detectors with synchrotron radiation allows *in situ* experiments during the growth of perovskite and other semiconductors. Relevant

information can be extracted from GISAXS scattering curves such as sizes, shapes, distances, and correlations of particles.[31,33,34] Such parameters are fundamental[32] in understanding the process of nucleation and growth.

In situ grazing incidence WAXS (GIWAXS) has been used to study the crystal structure during deposition, film formation, annealing, and degradation of perovskite solar cells, and there are already some review papers describing the results of employing *in/ex situ* X-ray scattering techniques on solution-based perovskites.[30,35] Barrows et al. reported an *in situ* GIWAXS/GISAXS characterization study on the formation of $MAPbI_{3-x}Cl_x$ during annealing. They followed the crystalline changes at 80 °C; at early stages, they observed only diffraction peaks related to crystalline precursors and until the 117th minute when the main diffraction peak (110) reached its maximum. However, they did not present an analysis of the GISAXS data beyond highlighting some variations in the Yoneda peak.[36] Zhong et al. reported an *in situ* GIWAXS study of $MAPbI_3$ crystallization deposited by blade coating. They found that at temperatures in the range of 80−100 °C the film dries fast and its composition is a mix of solvates, PbI_2 phases, and perovskite phases. However, at temperatures higher than 100 °C, there is a direct conversion to perovskite forming compact perovskite films.[37] In previous work by the authors, we reported the crystalline changes occurring during spin casting of $MAPbI_{3-x}Cl_x$ and $FAPbI_{3-x}Cl_x$ precursors by wide-angle X-ray scattering. The WAXS setup included a vertically positioned spin coater, which allows the incident X-ray beam and the substrate to be orthogonal probing the bulk film. It was found that during early stages of crystallization there was one-dimensional (1D) growth of an intermediate phase to form a crystalline perovskite precursor, which requires thermal annealing to form the desired crystalline perovskite.[38] Other GIWAXS studies such as Masi et al. reported time-resolved GIWAXS during crystallization of $MAPbI_3$ by multistep spin coating to study the effect of additives[39] and Tang et al. reported *in situ* GIWAXS measurements for different formamidinium perovskites at different temperatures of the substrates.[40] Most often, GIWAXS is reported when performing *in situ* grazing incidence X-ray scattering experiments and only a limited number of complementary *ex situ* GISAXS studies have been published for perovskites,[41,42] but it has been widely used to investigate in real-time different aspects of the crystallization of polymers,[43−46] metal nanoparticles,[23,47] or proteins.[48,49]

Additives can be used to control multiple properties, such as the crystallite size and density, and even provide control of the polymorph of a given species.[50] The presence of small concentrations of impurities or additives has no impact on the total volume, so nucleation continuously occurs throughout the majority of the solution. However, these impurities can enhance the nucleation rate acting as heterogeneous nucleation centers and have an important effect on the growing crystal structure.[51] Liang et al. reported the use of 1 wt % of DIO as an additive in the perovskite ink and they found that DIO increased the coverage and smoothness by stimulating heterogeneous nucleation and modifying the interfacial DIO perovskite precursor energy, making the crystals grow in contact with the surface. It is speculated that this is caused by the chelation of Pb^{2+}, with DIO affecting the dynamic equilibrium of the drying and annealing film and causing an increase in the internal energy and configurational entropy of the growing crystal, thus modulating the growth rate and the shape. As a result of the retarded crystallization upon adding DIO, the crystal growth is

defect-free.[7] Also, Lee et al. reported that DIO modifies the crystallization rate and enhances the formation of stable intermediate structures.[52] However, DIO can be removed with the solvent during the annealing process when using high temperature.[53]

The effect of HI as an additive in MAPbI$_3$ precursors was first reported by Heo et al., reaching an efficiency of 17.2%. They found that HI when used as an additive produced a perovskite film with fewer crystalline domains. HI enhances the solubility of PbCl$_2$/PbI$_2$, which favors the growth of continuous perovskite crystals during nucleation and growth, facilitating the formation of a dense pure perovskite.[54] HI can recover the methylamine (the decomposition product of MAI) back into MAI, thereby suppressing the decomposition reaction of MAPbI$_3$ perovskite.[6] Furthermore, there is no chemical reaction between HI and perovskite precursors, and HI is removed from the films during annealing.[55]

In this work, we investigate the influence of additives on the crystallization kinetics of methyl ammonium lead halide perovskites using *in situ* GISAXS and optical microscopy. Methyl ammonium lead halide perovskites formed from methyl ammonium lead chloride and lead iodide are known to be predominantly from methyl ammonium lead iodide.[38] *In situ* studies allow the growth process and the evolution of morphology to be monitored in real-time.[34] By combining scattering techniques and direct imaging, data collection at different stages of the crystallization process is possible. The results help in understanding the nucleation of mixed halide perovskite. Here, we focus on the influence of small quantities of additives, e.g., DIO and HI, on the nucleation and crystal growth processes, while in our previous report we imaged smaller length scales during the spin casting of MAPbI$_{3-x}$Cl$_x$ and FAPbI$_{3-x}$Cl$_x$ films.[38] The growth pathways followed during the film formation by bar-spreading perovskite ink are identified. Because of the fast process of crystallization of perovskites, *in situ* GISAXS was used to study the early stage of nucleation and growth, while *in situ* optical microscopy reveals the later growth stages of the perovskite crystals due to its limited resolution. These combined techniques enable *in situ* characterization throughout the entire process of the perovskite crystallization from the initial solvent evaporation to film formation. The growth mechanism is investigated by tracking the evolution of the size of the nuclei. We describe in detail the mechanism leading to the formation of the film morphology in bar-coated perovskites and propose a model based on the radius of gyration, power exponent, and effective radius. Additives indeed modify this process, accelerating the nucleation process and functioning as nucleation centers promoting heterogeneous nucleation. Furthermore, they play an important role in the morphology evolution. Regardless of the different scenarios of nucleation and growth, all of the MAPbI$_{3-x}$Cl$_x$ inks, with and without additives, deliver high-quality crystalline thin films.

2. EXPERIMENTAL METHODS

A perovskite precursor 3:1 MAI/PbCl$_2$ in 99.9% anhydrous dimethylformamide (DMF) was purchased from Ossila Ltd. Prior to deposition, the precursor solutions were continuously stirred and heated to 70 °C on a hot plate. The additive recipes used were taken from the literature: perovskite–DIO solution was prepared by adding 1 wt % of DIO with respect to the perovskite weight into the vial containing the solution and stirring overnight at 70 °C.[7] One percent per volume of HI was added to the perovskite precursor solution[56] for the perovskite–HI solution.

The glass substrates (Menzel-Glasser) were first sonicated for 10 min in hot water with Hellmanex solution (Z805939, Sigma-Aldrich) and then rinsed twice in boiling deionized water. After that, the substrates were again sonicated in isopropyl alcohol (IPA), followed by another rinse in deionized boiling water. They were then dried with compressed air, and finally the substrates were treated in an oxygen plasma cleaner for 10 min. During the bar spreading, 10 μL of perovskite ink was deposited on half a glass microscope slide (7.5 cm × 1.25 cm) using a bar speed of 40 mm s^{-1}. This speed allows the formation of a wet film within the Landau−Leviche regime. The same cleaning process and size of the silicon wafers were used in the GISAXS experiments.

Scanning electron microscopy (SEM) images were obtained using a JEOL Ltd. (Tokyo, Japan) JSM6010LA microscope. X-ray diffraction (XRD) patterns were obtained using a D2 Phaser Bruker diffractometer under monochromatic Cu Kα radiation (λ = 1.54184 Å) and on a range from 2θ = 5 to 60°.

2.1. *In Situ* GISAXS Experimental Setup. The bar coating system was transported to beamline i22 at the Diamond Light Source. The energy of the X-ray beam used was 14 keV, and the substrate was aligned to the beam with an incidence angle of α_i = 0.24°. For data acquisition, a Pilatus P3-2M detector was used at a distance of 9.504 m from the samples. Figure 1 shows a schematic representation of the
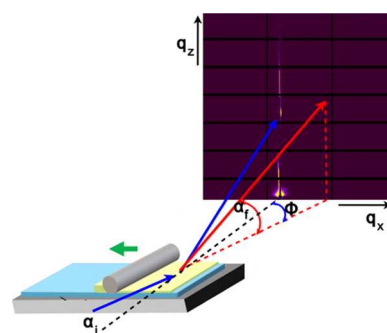
Figure 1. Schematic representation of the GISAXS setup for the bar coating system at the i22 beamline. The bar coating system was situated between the beam source and the detector, which was 9.504 m away from the sample.

GISAXS and bar coating setup. The precursor ink was deposited using a remotely controlled syringe pump. All measurements were performed following the same procedure; first, the substrate was aligned to the beam and held at 60 °C, and then the precursor ink was deposited using a syringe pump onto the silicon in front of the bar. During this time, the data from the X-ray detector was collected continuously; in total, 180 frames were taken before, during, and after spreading the ink over 3 min. While spreading the precursor ink, the bar momentarily blocked the X-ray beam. This was used to define the start of the process. The first meaningful data was observed immediately after the bar had passed through the beam. The detector recorded the intensity of scattered X-rays over a range of exit angles. Two beam stops were used: a circular stop where the straight-through beam is and a vertical strip to block the reflected beam and the intense vertical flare from the sample. The Yoneda peak position was identified by integrating along q_z a box profile, for all of the 2D GISAXS images in the stacks. Once the Yoneda peak position was identified, another box profile along q_y was drawn to extract intensity profiles. The GISAXS processing was performed using DAWN software and the fitting using SasView.

2.2. *In Situ* Microscopy Setup. A Nikon LP-EPILED microscope with a Pixelink PL-B742FF camera was attached above a bar coating system to observe the kinetics of crystallization of the perovskite solution. Immediately after spreading the perovskite inks, the lens was lowered in place and the focus was adjusted to observe the perovskite ink as it dries at the center of the glass substrate. Lenses with 40× and 60× magnifications were used. The image stacks were processed and analyzed by ImageJ-FIJI to extract the number of crystals, spatial distribution (40× magnification), and area of the crystals (60×
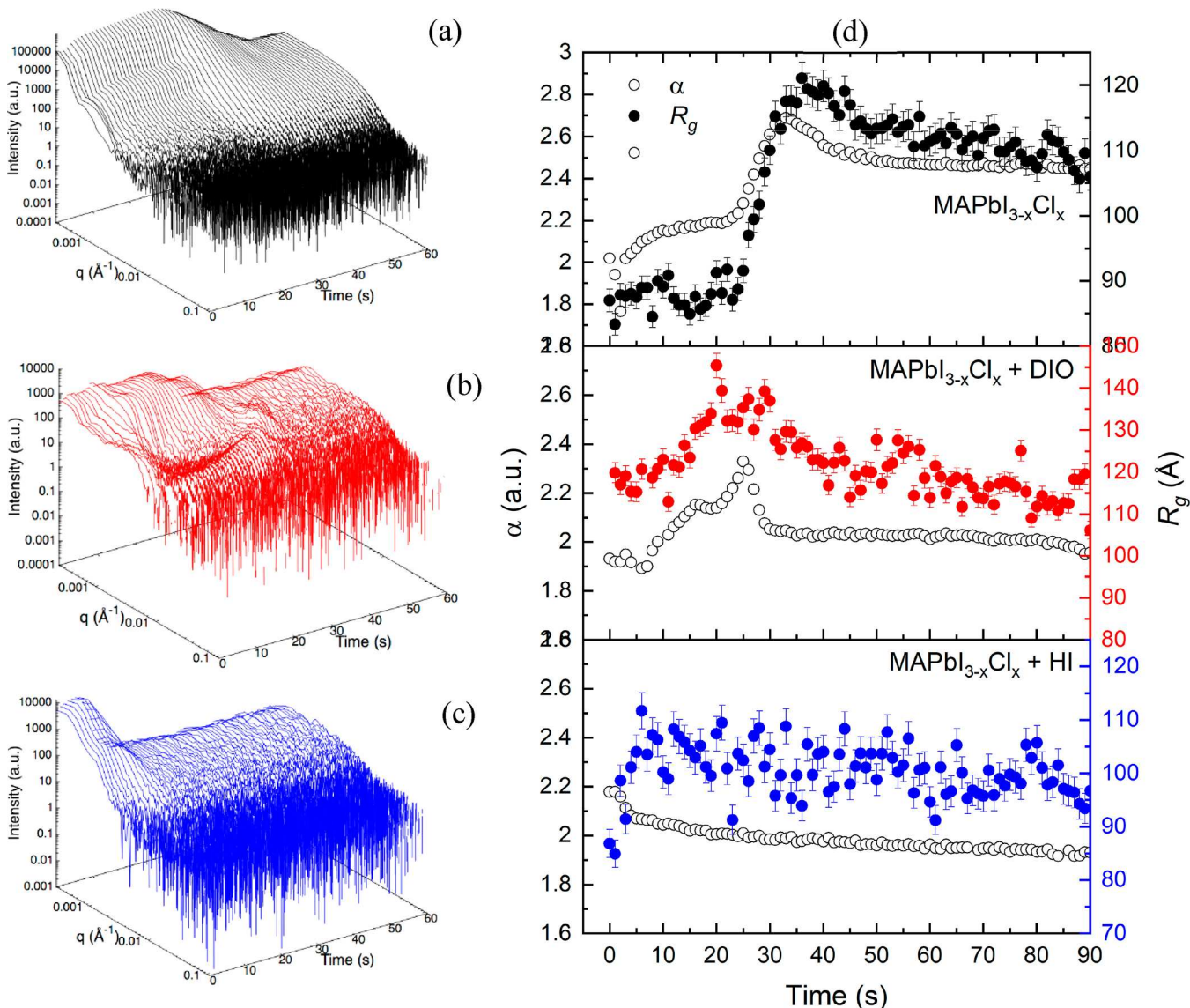
Figure 2. GISAXS scattering profiles of (a) MAPbI$_{3-x}$Cl$_x$, (b) MAPbI$_{3-x}$Cl$_x$ + DIO, (c) MAPbI$_{3-x}$Cl$_x$ + HI, and (d) evolution of α and R_g of MAPbI$_{3-x}$Cl$_x$ and with additives.

magnification) (see Figures S4−S6 for details of the image analysis algorithms).

3. RESULTS AND DISCUSSION

3.1. Crystallization as Followed by *In Situ* GISAXS.
Figure 2a−c shows the GISAXS profiles along the Yoneda peak during the bar spreading of the various precursor inks. The X-ray scattering data was fitted with a power law model and analyzed using Guinier's law ($I(q) = \rho_0^2 v^2 \exp(-1/3q^2R_g^2)$), where $I(q)$ is the scattering intensity, R_g is the radius of gyration, ρ_0 is the average scattering length density, and v is the volume of the particle. Guinier's law suggests that the plot $I(q)$ vs q^2 gives the initial slope $(R_g/3)$[57] to determine the particle size evolution during the process of nucleation. The data was also analyzed using a power law model described by $I(q) = scale*q^{-\alpha} +$ background, where α is the power; this calculates a simple power law with a flat background.[57] Both the radii of gyration and the power exponent were determined, and Figure 2d shows the evolution of α and R_g for MAPbI$_{3-x}$Cl$_x$ with additives at $T_{sub} = 60$ °C.

The MAPbI$_{3-x}$Cl$_x$ profiles present three changes in their intensity and shape: in stage 1, from the beginning of the experiment to ∼25 s, there is a slight increase in the intensity at $q \sim 0.001$ Å^{-1}. This increase in the intensity at intermediate q values may be associated with mainly heterogeneous nucleation and to a lesser extent homogeneous nucleation.[58] In stage 2, from ∼25 to ∼30 s, the profiles reach a maximum, after which the feature at $q \sim 0.001$ Å^{-1} dissipates, and in stage 3, after ∼30 s, the intensity of the scattering profiles decreases until 50 s after which time it remains constant and holds the same shape for the rest of the GISAXS experiment. It can therefore be reasonably assumed that these changes in the intensity of the profiles are related to the clustering, nucleation, and then aggregation of perovskite precursors. These three stages are also witnessed in the power law exponent α values: from $\alpha = 1.9$ to 2.2 in ∼25 s (stage 1) to continue growing to a maximum $\alpha = 2.7$ at ∼33 s (stage 2) and then α decreases to remain at a constant value during the rest of the experiment at values close to $\alpha = 2.45$ (stage 3) (see Figure 2d). When α remains constant, it is assumed that most of the solvent has evaporated and the $I(q)$

profile then remains almost the same, indicating that the perovskite films have formed. The increase in the scattering intensity in the early stages of the *in situ* GISAXS experiment has previously been related to the formation of primary particles by observing a power law behavior,[58] and the decrease in the exponent of the power law is associated with a change in the aggregation state of the particles. Similar phenomena are thought to occur in the perovskite system studied here, where the aggregation state initially changes and then stabilizes when α reaches a maximum after which it remains constant during the rest of the experiment.

In situ GISAXS was also used to study the influence of a small amount of additives in the perovskite ink; 1 wt % of DIO and 1% per volume of HI were added to the ink solution. In contrast, a more complex behavior is observed in the presence of DIO in MAPbI$_{3-x}$Cl$_x$, as shown in Figure 2b. A feature at $q \sim 0.01$ Å^{-1} is formed, which gradually shifts to lower q values up until 30 s and finally it disappears at $q \sim 0.003$ Å^{-1}. Additionally, another shoulder at low $q \sim 0.001$ Å^{-1} is present. After ~35 s, the profiles reduce their intensity and they keep the same shape. In the presence of DIO, α values change from 1.9 at ~5 s to $\alpha = 2.1$ at ~22 s in a first increase; then, after keeping a constant value for a few seconds, this value grows sharply to a maximum value of $\alpha = 2.3$ (~30 s). Once α has reached the maximum, it suddenly decreases to 2.0 and it has the same value during the rest of the experiment. More rapid changes are observed when HI is added, as shown in Figure 2c; first, the scattering intensity is high and sharply decreases in just less than ~10 s and then remains the same shape during the rest of the experiment. Similarly, α changes from $\alpha = 2$ to 2.17 and then decreases again to values around. The fast changes suggest rapid crystallization and drying of the solvent forming a solid film when HI is present.

Most of the α values are in the range of $2 \leq \alpha \leq 3$, which corresponds to particles or films with surface fractal characteristics, i.e., they correspond to objects that possess a rough surface and exhibit fractal properties. Films with surface fractals possess 2D self-similar morphology on different scales from nanometers to micrometers, which implies that the film contains densely packed perovskite grains.[59] The changes in α and the fractal dimension $D_s = 6 - \alpha$ can tell us about the transformations on the surface roughness during the different phases of nucleation. An increase in D_s indicates that the surface roughness becomes larger.[59] MAPbI$_{3-x}$Cl$_x$ nuclei experience a reduction in the surface roughness as a consequence of the aggregation of the perovskite precursors forming a more compact film. On the contrary, when HI is present in the ink, the roughness increases as D_s escalates from 3.72 to 4.1 during the experiment; similar values are observed for DIO (see Figure S2).

Figure 2d shows the evolution of α and R_g for MAPbI$_{3-x}$Cl$_x$ and MAPbI$_{3-x}$Cl$_x$ with additives at $T_{sub} = 60$ °C. For the pristine MAPbI$_{3-x}$Cl$_x$ ink, R_g is determined to be 90 Å for the first 25 s and then increases sharply to a maximum $R_g = 126$ Å at 35 s and to 111 Å at 90 s and ~100 Å (150 s) to continue varying only slightly during the rest of the experiment. A feature is observed at 0.001 Å^{-1} in the intensity profiles, attributed to clusters/nuclei of larger than ~6000 Å during the 24 s of the nucleation process, while the Guinier analysis shows clusters/nuclei with gyration radii of hundreds of Å.

The presence of additives modifies the trend of R_g values; in the presence of additives, R_g starts to grow almost immediately to a maximum value where it remains, whereas without any additives, there appears to be a longer induction time before it starts to grow. For MAPbI$_{3-x}$Cl$_x$ + DIO, the initial R_g value

detected is around 120 Å and reaches a maximum $R_g = 144$ Å after 20 s. In addition to the calculated R_g value, a feature at mid-range q values is also observed in the scattering profiles of MAPbI$_{3-x}$Cl$_x$ + DIO, observed with a maximum at 0.0122 Å^{-1} and moving to lower q values at $q = 0.0013$ Å^{-1} to later finally disappear due to the aggregation of the particles into larger crystals. When HI is present, R_g values grow in the first 10 s from 86 to 110 Å. The trends observed in the evolution of R_g imply the existence of an induction time that is decreased by the presence of the additives, which accelerates the process of nucleation until R_g reaches the maximum value. Once R_g reaches its peak value, it slowly reduces over time; this decline in R_g is believed to correspond to the creation of a solid thin film from which the final residual solvent is evaporating at which point the Guinier analysis is no longer applicable.

The evolution of α and R_g is expected to grow in a similar fashion.[46] An induction time is also observed in the evolution of α; the growth of α occurs earlier for the ink with additives than for the pristine. What stands out is the faster growth of MAPbI$_{3-x}$Cl$_x$ + HI compared to that of any other ink; HI is a very effective nucleating agent, and the crystallization forms rapidly; consequently, it is thought that just the partial growth of the film formation was imaged.

Growth mechanisms can be studied by tracking the size evolution of the nucleation centers; the LSW theory states that the particle growth as a function of time should follow $\sim t^x$. This approach has been extended to perovskite nucleation from nanoparticle systems.[23−25] Figure 3 shows a log−log plot of R_g as
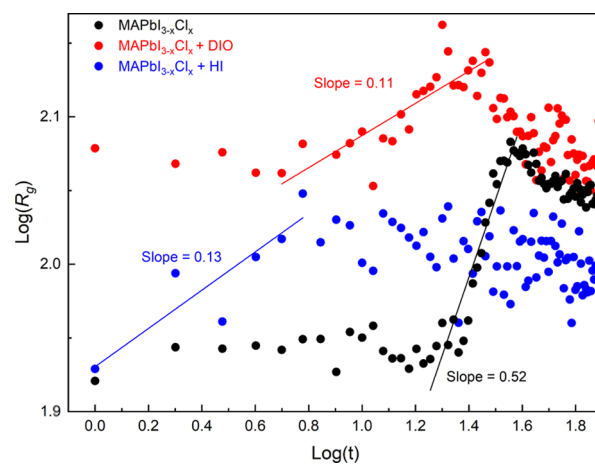
Figure 3. Log−log plot of the evolution of R_g. Power law fitting was performed in the range of sharp increase in R_g, and they are indicated by the straight lines, for MAPbI$_{3-x}$Cl$_x$ $R_g \sim t^{1/3}$, MAPbI$_{3-x}$Cl$_x$ + DIO $R_g \sim t^{0.11}$, and MAPbI$_{3-x}$Cl$_x$ $R_g \sim t^{0.13}$.

a function of time for the pristine MAPbI$_{3-x}$Cl$_x$ and with each of the additives. By fitting the section of the data set where the R_g values are increasing, it is shown that the R_g of the pristine MAPbI$_{3-x}$Cl$_x$ grows as $\sim t^{0.52}$ following a reaction-limited process ($\sim t^{1/2}$). Under this mechanism, the perovskite crystals obey a classic crystallization and they grow slowly. Basically, nuclei are surrounded by the solution that is supplying precursors to deposit on the surfaces of the nuclei forming polyhedral crystals.[60,61] Diffusion-limited growth would in theory follow a $\sim t^{1/3}$ growth; our results show a notably lower power exponent; R_g of DIO and HI grow as $\sim t^{0.11}$ and $\sim t^{0.13}$, respectively. Similar trends have been previously observed by Woehl et al. and attributed to hindered diffusion-limited
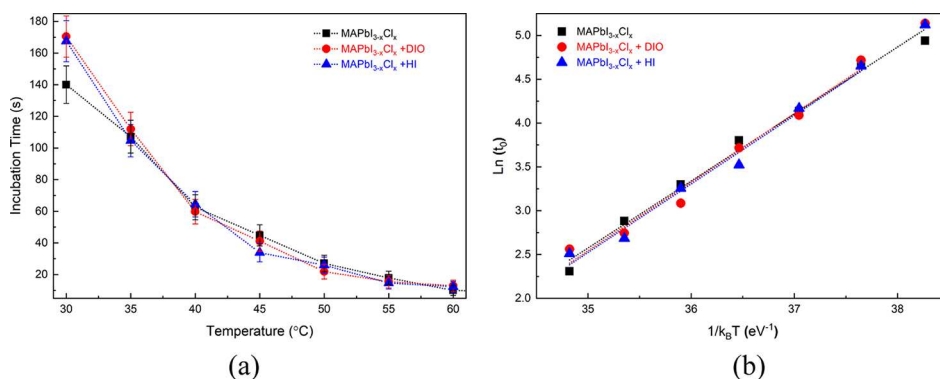
Figure 4. (a) Incubation time and (b) Arrhenius plot to determine E_a. The slope for the pristine precursor is 73.78 ± 2.89 kJ mol^{-1}, for + DIO, it is 75.61 ± 2.89 kJ mol^{-1}, and for + HI, it is 75.41 ± 3.85 kJ mol^{-1}.

growth[62] due to either multiparticle effects or attached growth. Therefore, in our experiments, it is highly possible that both additives experienced hindered diffusion-limited growth with even smaller t^x than with the theoretical $t^{1/3}$ due to a large number of nuclei. Another possible explanation for this might be the uncertainty in the measurement of R_g being greater for the DIO and HI samples due to the rapid nucleation, which means there were fewer data points available in the region of interest when fitting in the log−log plot. In hindered diffusion-limited growth, there is a high number of nuclei and it is highly probable that nuclei grow upon collision and then aggregate, reducing the total surface energy resulting in a concentration gradient around the nuclei reaching a diffusion-limited state.[60,61]

3.2. Crystal Growth as Observed by Optical Microscopy. An isothermal study at 60 °C was performed to directly observe the dynamic crystallization of MAPbI$_{3-x}$Cl$_x$ perovskite by *in situ* optical microscopy. Wet films were formed after the precursor ink was spread by bar coating. Optical microscopy can detect crystals and follow their growth at length scales larger than ~1 μm, complementing the GISAXS experiment that probes shorter length scales. Two lenses of different magnifications (40× and 60×) were used; the pixel size at 40× is 5.45 μm pixel^{-1} and at 60× is 3.59 μm pixel^{-1}. The former was used to study the number of particles and the latter was used to observe the area of the crystals.

What is interesting about the Supporting Information videos of the perovskite crystallization is that some crystals were growing in fixed locations and others were initially moving to later remain fixed or to attach to other fixed crystals, suggesting that nucleation is occurring in both the bulk and potentially at the system boundaries for these perovskite films. When the wet film has reached the supersaturation state, crystals nucleate directly from the solution ink forming crystals and later form a film over the substrate. Once the crystals have reached their maximum size, they form a film and subsequently turn dark in color, indicating the complete evaporation of the solvent (DMF). However, these initial crystals correspond to intermediate phases or precursor−solvent phases, which only after adequate annealing form the desirable tetragonal perovskite structures.

The first parameter taken from the stack of images without any calculation or image processing is the incubation time t_0, defined here as the time required for the first crystal to grow large enough to be observed by microscope, which depends on the magnification used.[63] Figure 4a shows t_0 for the pristine perovskite ink and the inks with additives; as the temperatures increase, t_0 decreases when an objective of 40× magnification is

used. Higher temperatures needed less time to reach the saturation point required to initiate the crystallization. From Figure 4b, the activation energy E_a for the formation of these crystalline intermediate phases can be calculated by the slope of an Arrhenius plot Int_0 vs $1/k_BT$.[63] E_a values calculated here are slightly increased by the presence of the additives, and these values correspond to the formation of an MAPbI$_{3-x}$Cl$_x$ intermediate. The E_a value for the pristine precursor is 73.78 ± 2.89 kJ mol^{-1}; E_a increases to 75.61 ± 2.89 kJ mol^{-1} when DIO is added and 75.41 ± 3.85 kJ mol^{-1} for HI. Other studies have reported the E_a values for different deposition techniques and employed different methodologies for the calculation of E_a for annealed perovskites, e.g., for spin coating, a value of $E_a = 85$ kJ mol^{-1} was reported using PbCl$_2$ as a precursor,[5] and for a slot-die deposition technique, a value of $E_a = 81.4$ kJ mol^{-1} was used,[64,65] which is in the same order of magnitude to the E_a values calculated for bar coating under ambient conditions. Another parameter that affects E_a reported by Moore et al. is humidity from the local environment that accelerates the crystallization and decomposition of perovskites; then, the activation energy of nucleation and growth is likely higher for films coated in an inert environment. They also reported that a high E_a value requires a longer period of time for the solvent to evaporate and a lower E_a reduces the period of coarsening and a very low E_a results in poor film morphology.[66]

The time dependence of the number and size of crystals is further analyzed. An image analysis algorithm was used to obtain the number of crystals N_p and the average size of the crystals r_{eff} over time. Figure 5 shows the evolution of the number of crystals for the pristine MAPbI$_{3-x}$Cl$_x$ and with additives at $T_{sub} = 60$ °C. DIO and HI cause the generation of more nuclei and they appear sooner. HI shows the most dramatic change relative to the pristine MAPbI$_{3-x}$Cl$_x$ followed by DIO. In addition to this, after the number of crystals reached their maximum, N_p continues falling due to possible events of aggregation or Ostwald ripening phenomena as well as collision with other crystals, represented as open circles in Figure 5. The N_p data presented here does not consider these aggregation events due to their complexity and therefore only data from the early part of the process, i.e., before it starts to decrease, is considered.

According to the data in Figure 5, we can infer that the increase in N_p is due to the small amounts of either of the additives dispersed through Brownian motion in the wet film, functioning as nucleation centers for the process of heterogeneous nucleation synchronously occurring with homogeneous nucleation. The additive surface decreases the barriers to nucleation because of the reduction of the interfacial free energy.
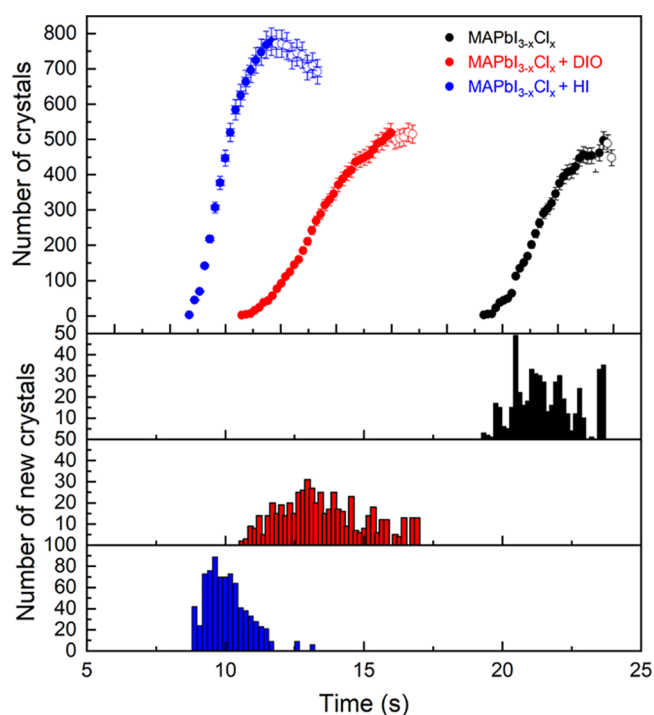
Figure 5. Evolution of the number of particles N_p for MAPbI$_{3-x}$Cl$_x$ and additives. The plots at the bottom show the number of new particles appearing for every frame.

The presence of these entities could be associated with the nucleation mechanism of saturation by pre-existing nuclei. Notwithstanding, if there are pre-formed nuclei (PbI$_2$−DMF or MAPbI$_{3-x}$Cl$_x$−additive−DMF complexes), they cannot be detected and differentiated at the magnification used. Figure 5 also shows histograms of new crystals as a function of time for each ink, indicating that none of the inks present a continuous rate of growth.

To further understand the growth kinetics of mixed halide perovskite deposited by bar coating, the growth of crystals was observed by real-time optical microscopy using a 60× magnification lens; Figure 6 shows selected images of the perovskite crystal evolution at T_{sub} = 60 °C, and the complete stacks are available as a video in the Supporting Information. To compare the evolution of the crystal size, the effective radius is defined as the square root of the area $r_{eff} = \sqrt{A}$ to permit comparison directly between the complex nonspherical crystal shapes. For the pristine ink, the crystals are in the shape of plate dendrites and more complex morphologies, dendrites with branches. These more complex structures are more commonly observed when the temperature is increased. When the additives are incorporated into the perovskite ink, the shapes take on different forms, which are visible to the naked eye on the later growth and the crystal size is smaller than the pristine MAPbI$_{3-x}$Cl$_x$. For DIO, there is a combination of crosses and some circular plate crystals appearing later. Finally, for HI, the crystals are complex shapes; it was not possible to resolve the
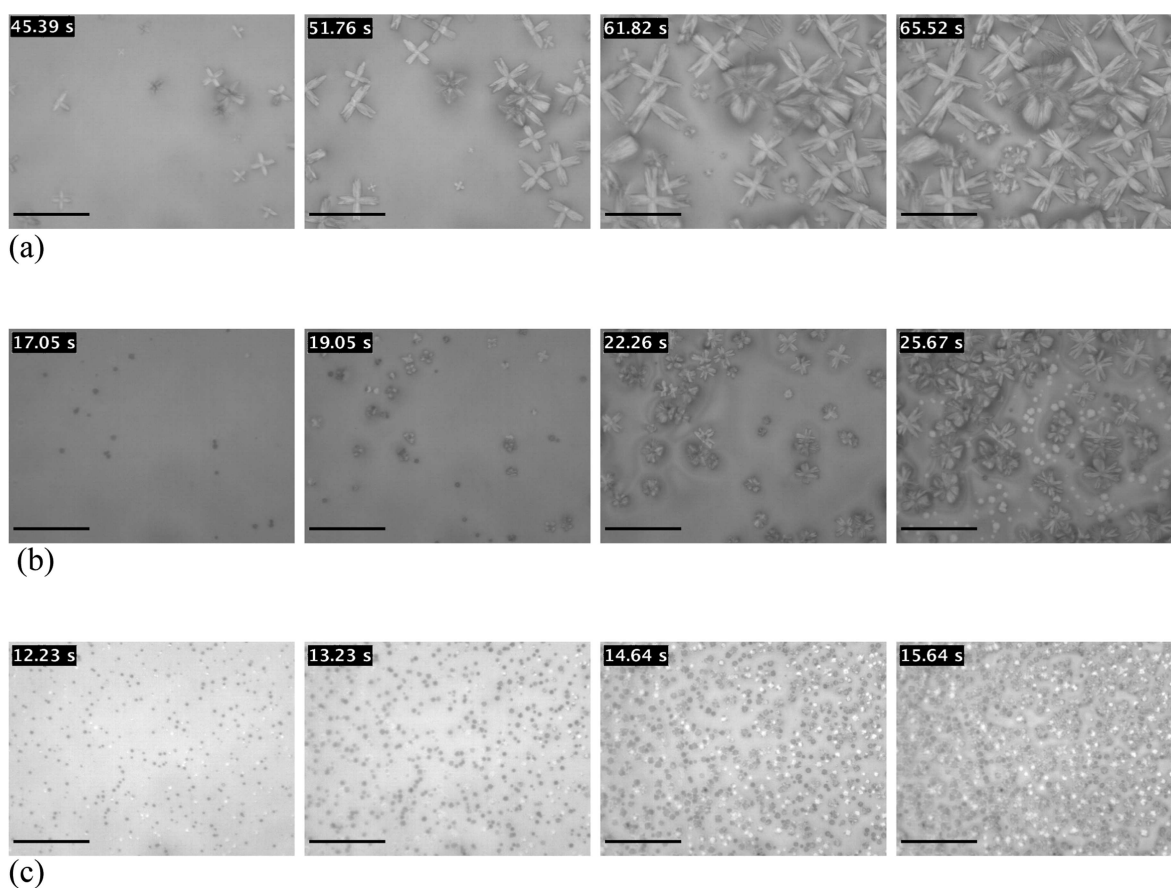

Figure 6. Real-time sequence of images at 60× at T_{sub} = 60 °C of (a) MAPbI$_{3-x}$Cl$_x$, (b) MAPbI$_{3-x}$Cl$_x$ + DIO, and (c) MAPbI$_{3-x}$Cl$_x$ + HI. The scale bar is 50 μm in all of the images.

structure in detail because of the very small features with the magnification used but only roundish crystals are observed.

The spatial location of the nucleation seed of the crystal was transformed into a Voronoi tessellation to estimate the size distribution of the crystals when N_p has reached a maximum value (see Figure S6). Each Voronoi space is considered as an approximation of the final area of the crystals before forming a film. Figure 7 shows the normal distributions of r_{eff} calculated
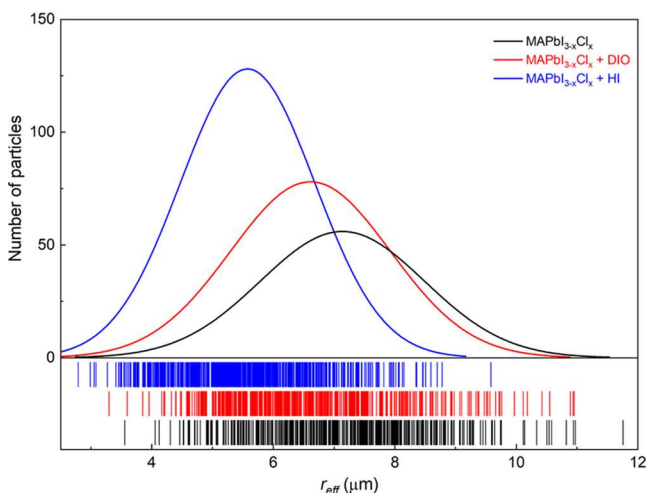
Figure 7. Particle size distribution of MAPbI$_{3-x}$Cl$_x$ and with additives.

from the Voronoi diagrams; indeed, an inverse relation of r_{eff} and N_p is observed, whereby low N_p is associated with large r_{eff}. The presence of additives decreases r_{eff} from an average of 7.26 ± 1.35 to 6.74 ± 1.31 μm in the presence of DIO and to 5.68 ± 1.10 μm when HI is added.

Five or more crystals were selected from the sequence of images taken at 60× magnification and processed to calculate the area of the crystal over time; the rate for each individual crystal is shown in Figure S7 in the Supporting Information. The sizes r_{eff} of individual crystals confirm the same trend as the Voronoi approximation; r_{eff} of pristine MAPbI$_{3-x}$Cl$_x$ grows larger in size than MAPbI$_{3-x}$Cl$_x$ + HI and MAPbI$_{3-x}$Cl$_x$ + DIO. The growth rate calculated is directly proportional to the total flux of precursors or nuclei joining the crystals.[67]

The rate of growth showed a different rate for each individual crystal; an average of the pristine perovskite is around ~1.33 ± 0.15 μm s^{-1}. On the contrary, DIO and HI slightly accelerate this process to ~1.37 ± 0.37 and ~1.36 ± 0.34 μm s^{-1}, respectively. Indeed, independent of the precursor composition, the growth rate of the crystals is linear due to the fact that the solute density changes in the crystallization regime and can be estimated as steady when the solute diffusion rate is similar to the solute crystallization rate.

The size of the perovskite crystals is governed by the spatial distribution of the nuclei, the number of nuclei, and the temperature of the substrate, while a low number of nuclei facilitates the growth of larger sized crystals due to the lack of competitors for nuclei precursor.[68] On the contrary, when N_p is high, the new crystals have to compete with the already existing neighbor crystals to accumulate more material resulting in perovskite precursors having a smaller final size. At temperatures close to ambient conditions, the lower nucleation density helps to grow large crystals due to fewer competitors for solutes.[68] Also, at low supersaturation, the barrier energy is relatively large;

hence, the appearance of particles with sizes larger than the critical radius is less probable and just a few crystals are formed. As the temperature increases, the number of crystals increases. At 60 °C, it was observed that when the number of crystals is high, the size is smaller due to the free energy of the system being distributed in all of the crystals and it is shared among many small crystals rather than just a few large crystals. Furthermore, at high supersaturation, the energy barrier for a change of phase diminishes and the number of new particles is even larger. Moreover, based on the real-time observation of the crystal growth, the final size of the mixed halide is the product of a combination of factors such as nucleation density, speed of deposition, and temperature of the substrate, and indeed, the additives have a profound effect on the nucleation and growth of mixed halide perovskites.

During the process of deposition and supersaturation, the wet film may contain a distribution of clusters, nuclei, and crystals of the perovskite precursors, which all may play a particular role in the nucleation and growth, making identification of the main actor in the process of crystallization difficult. To determine the crystal structures present, XRD was performed on unannealed and annealed MAPbI$_{3-x}$Cl$_x$ samples (see Figure 8). The
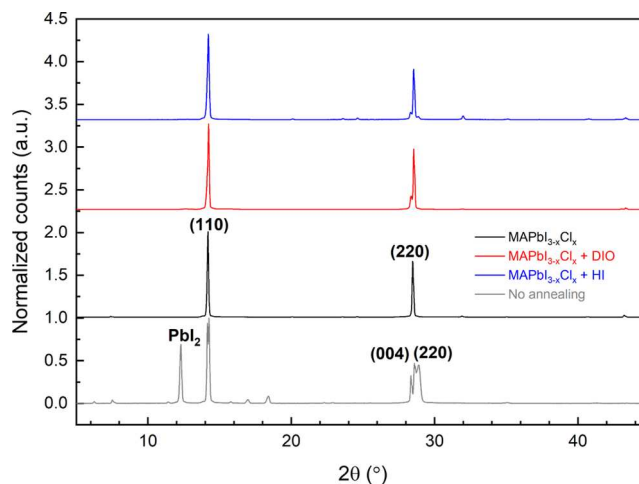
Figure 8. XRD patterns of unannealed (T_{sub} = 60 °C) and annealed MAPbI$_{3-x}$Cl$_x$ samples (T_{sub} = 60 °C and annealed for 1 h at 90 °C followed by another hour at 100 °C).

unannealed XRD pattern shows the different peaks from PbI$_2$; (110), (004), and (220) planes arise from the background.[36] Thus, during the GISAXS and optical microscopy experiments, an intermediate phase composed of crystalline PbI$_2$ and perovskite precursors was analyzed. The structural behavior behind the crystallization of MAPbI$_{3-x}$Cl$_x$ has been deciphered by Stone et al. and in agreement with our previous report[38] where it was found that the precursor film is formed by 1D chains of MA$_2$PbI$_3$Cl coexisting with disordered MACl. The former forms a pinhole-free film, while the latter dramatically hinders the formation of MAPbI$_{3-x}$Cl$_x$ and it must first evaporate before the MA$_2$PbI$_3$Cl converts to perovskite and yet more MACl, which is liberated as a gas. The conversion process to perovskite is slowed by the time taken for the disordered MACl to evaporate.[38,69] In contrast, the annealed sample shows a strong preferential orientation along the (110) and (220) planes, suggesting a complete formation of the tetragonal perovskite structure. Blade-coated or bar-coated perovskites also require long annealing times e.g., 1 h at 90 °C
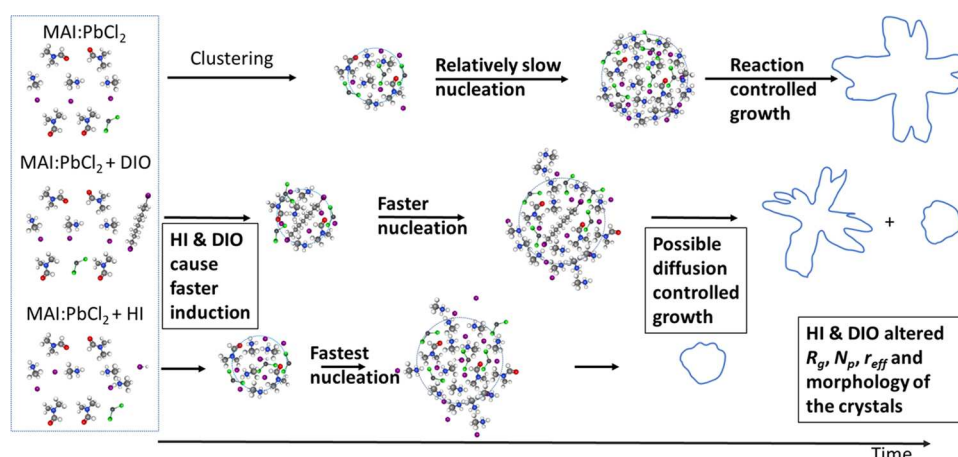
Figure 9. Schematic representation of the nucleation and growth process of perovskites. After the ink has been spread, a wet film is formed. First, the perovskite precursors cluster, and once their radius is larger than the critical radius, they keep growing until they reach a maximum R_g. Finally, the nuclei function as elemental units in the growth of the perovskite crystals. The presence of the additives accelerates the nucleation and affects the morphology of the nuclei.

followed by another hour at 100 °C,[70] to fulfill the tetragonal perovskite phase due to the presence of disordered MACl in the process of film formation. As shown in Figure 8, the influence of the additives on the final crystal structure formed is null; all annealed samples present the same tetragonal phase, but the film morphology varies significantly as evidenced by the microscopy, confirming that the additives just have an impact on the process of nucleation and growth of mixed halide perovskite but not on the crystalline packing.

3.3. Mechanism of Nucleation and Growth. The interpretation of the nucleation and growth is challenging; these processes were divided into a series of stages based on the real-time results presented above, and by considering the understanding obtained from the overlapping parameters obtained from the power law fitting, Guinier analysis, and the effective radius from both optical microscopy and GISAXS, a crystallization mechanism is proposed in Figure 9. The very earliest formation probably follows a similar low-dimensional process (possibly 1D) as shown for *in situ* spin casting.[38] At the induction time, precursors start forming clusters. Once R_g is larger than the critical radius, individual stable nuclei continue growing. As shown by GISAXS for the additive-free films, the growth follows a reaction-limited process, whereas the films with additives follow a hindered diffusion-limited growth (presumably due to the very large number of nucleation sites). Then, those nuclei reach a maximum R_g and they start forming crystals of larger length scales through aggregation. The induction time is diminished by the presence of DIO or HI, just as the incubation time observed by the optical microscopy is reduced. Furthermore, a slow nucleation results in reaction-controlled growth; in contrast, a fast nucleation will follow a hindered diffusion-controlled growth of mixed halide perovskite. Finally, as observed in the optical microscopy, the growth of the perovskite crystals continues with r_{eff} following a linear trend of lateral growth independent of the precursor composition.

4. CONCLUSIONS

In summary, we studied the crystallization of mixed halide perovskites by bar coating under ambient conditions in real-time using optical microscopy and GISAXS. The laboratory-scale bar deposition system can be used to fabricate high-quality perovskite thin films, narrowing the gap between industrial-

scale production and research laboratory experiments, while also reducing the waste of precursors during deposition.

Significantly different kinetics were caused by the presence of DIO or HI, which speed up the nucleation, increasing the number of crystals, affecting their morphology, and promoting heterogeneous nucleation. Nevertheless, the small amounts of additives used do not alter the crystalline packing of perovskites in the final thin films. The presence of the additives, e.g., DIO and HI, changes the speed of the nucleation along with the mode of growth from reaction-controlled growth for the pristine $MAPbI_{3-x}Cl_x$, which follows an $\sim t_{0.52}$ power law to a possibly hindered diffusion-controlled growth in the presence of HI and DIO, which grow following an $\sim t_{0.13}$ and $\sim t_{0.11}$ power laws. Crystal size evolution of mixed halide perovskites studied by real-time optical microscopy late in the growth process showed that the effective radius of the crystals constrained within the thinning film as the solvent evaporates followed a linear pattern of lateral growth independent of the precursor composition. This study has gone some way toward enhancing our understanding of nucleation and growth of mixed halide perovskites under ambient conditions.

ASSOCIATED CONTENT

Ⓢ Supporting Information

The Supporting Information is available free of charge at https://pubs.acs.org/doi/10.1021/acsaem.0c02625.

    Video taken by an optical microscope at 60× magnification during crystallization for $MAPbI_{3-x}Cl_x$ (MP4)

    Video taken by an optical microscope at 60× magnification during crystallization for $MAPbI_{3-x}Cl_x$ + DIO (MP4)

    Video taken by an optical microscope at 60× magnification during crystallization for $MAPbI_{3-x}Cl_x$ + HI (MP4)

    Details of the Guinier analysis and fittings performed on the radius of gyration and effective radius; details of the image processing for images taken at 60× and 40× magnifications and to calculate the Voronoi diagrams; and SEM images of unannealed and annealed mixed halide perovskite films (PDF)

AUTHOR INFORMATION

Corresponding Author

Edwin Pineda De La O − *Chemical and Biological Engineering, The University of Sheffield, Mappin St, Sheffield S1 3JD, U.K.;* orcid.org/0000-0003-0508-3573; Email: ep.de.la.o@ msn.com

Authors

Noura Alhazmi − *Chemical and Biological Engineering, The University of Sheffield, Mappin St, Sheffield S1 3JD, U.K.*

Stephen J. Ebbens − *Chemical and Biological Engineering, The University of Sheffield, Mappin St, Sheffield S1 3JD, U.K.;* orcid.org/0000-0002-4727-4426

Alan D. F. Dunbar − *Chemical and Biological Engineering, The University of Sheffield, Mappin St, Sheffield S1 3JD, U.K.;* orcid.org/0000-0002-2313-4234

Complete contact information is available at:
https://pubs.acs.org/10.1021/acsaem.0c02625

Author Contributions

The manuscript was written through contributions of all authors. All authors have given approval to the final version of the manuscript.

Notes

The authors declare no competing financial interest.

REFERENCES

(1) Laboratory, N. R. E. Best Research-Cell Efficiency Chart, https://www.nrel.gov/pv/cell-efficiency.html ((accessed Aug 10, 2020).

(2) Kim, J. H.; Jung, J. W.; Williams, S. T.; Liu, F.; Russell, T. P.; Jen, A. K.-Y. Enhanced Crystalline Morphology of a Ladder-Type Polymer Bulk-Heterojunction Device by Blade-Coating. *Nanoscale* **2015**, *7*, 10936−10939.

(3) Xiao, Z.; Dong, Q.; Bi, C.; Shao, Y.; Yuan, Y.; Huang, J. Solvent Annealing of Perovskite-Induced Crystal Growth for Photovoltaic-Device Efficiency Enhancement. *Adv. Mater.* **2014**, *26*, 6503−6509.

(4) Yang, W. S.; Noh, J. H.; Jeon, N. J.; Kim, Y. C.; Ryu, S.; Seo, J.; Seok, S. Il. High-Performance Photovoltaic Perovskite Layers Fabricated through Intramolecular Exchange. *Science* **2015**, *348*, 1234−1237.

(5) Barrows, A. T. Novel Materials and Deposition Techniques for Solution Processed Solar Cells. Ph.D. Thesis, 2015.

(6) Heo, J. H.; Han, H. J.; Kim, D.; Ahn, T. K.; Im, S. H. Hysteresis-Less Inverted CH3NH3PbI3 Planar Perovskite Hybrid Solar Cells with 18.1% Power Conversion Efficiency. *Energy Environ. Sci.* **2015**, *8*, 1602−1608.

(7) Liang, P. W.; Liao, C. Y.; Chueh, C. C.; Zuo, F.; Williams, S. T.; Xin, X. K.; Lin, J.; Jen, A. K. Y. Additive Enhanced Crystallization of Solution-Processed Perovskite for Highly Efficient Planar-Heterojunction Solar Cells. *Adv. Mater.* **2014**, *26*, 3748−3754.

(8) Boopathi, K. M.; Mohan, R.; Huang, T.-Y.; Budiawan, W.; Lin, M.-Y.; Lee, C.-H.; Ho, K.-C.; Chu, C.-W. Synergistic Improvements in Stability and Performance of Lead Iodide Perovskite Solar Cells Incorporating Salt Additives. *J. Mater. Chem. A* **2016**, *4*, 1591−1597.

(9) Chiang, C.-H.; Wu, C. G. Bulk Heterojunction Perovskite-PCBM Solar Cells with High Fill Factor. *Nat. Photonics* **2016**, *10*, 196−200.

(10) Liu, S.; Guan, Y.; Sheng, Y.; Hu, Y.; Rong, Y.; Mei, A.; Han, H. A Review on Additives for Halide Perovskite Solar Cells. *Adv. Energy Mater.* **2020**, *10*, No. 1902492.

(11) Kim, H. B.; Choi, H.; Jeong, J.; Kim, S.; Walker, B.; Song, S.; Kim, J. Y. Mixed Solvents for the Optimization of Morphology in Solution-Processed, Inverted-Type Perovskite/Fullerene Hybrid Solar Cells. *Nanoscale* **2014**, *6*, 6679−6683.

(12) Wang, Q.; Shao, Y.; Dong, Q.; Xiao, Z.; Yuan, Y.; Huang, J. Large Fill-Factor Bilayer Iodine Perovskite Solar Cells Fabricated by a Low-Temperature Solution-Process. *Energy Environ. Sci.* **2014**, *7*, 2359.

(13) Jeon, N. J.; Noh, J. H.; Kim, Y. C.; Yang, W. S.; Ryu, S.; Seok, S. Il. Solvent Engineering for High-Performance Inorganic-Organic Hybrid Perovskite Solar Cells. *Nat. Mater.* **2014**, *13*, 897.

(14) Nie, W.; Tsai, H.; Asadpour, R.; Blancon, J. C.; Neukirch, A. J.; Gupta, G.; Crochet, J. J.; Chhowalla, M.; Tretiak, S.; Alam, M. A.; Wang, H. L.; Mohite, A. D. High-Efficiency Solution-Processed Perovskite Solar Cells with Millimeter-Scale Grains. *Science* **2015**, *347*, 522−525.

(15) Yang, L.; Barrows, A. T.; Lidzey, D. G.; Wang, T. Recent Progress and Challenges of Organometal Halide Perovskite Solar Cells. *Rep. Prog. Phys.* **2016**, *79*, No. 026501.

(16) Zhang, F.; Zhu, K. Additive Engineering for Efficient and Stable Perovskite Solar Cells. *Adv. Energy Mater.* **2020**, *10*, No. 1902579.

(17) Jena, A. K.; Kulkarni, A.; Miyasaka, T. Halide Perovskite Photovoltaics: Background, Status, and Future Prospects. *Chem. Rev.* **2019**, *119*, 3036−3103.

(18) Lovette, M. A.; Browning, A. R.; Griffin, D. W.; Sizemore, J. P.; Snyder, R. C.; Doherty, M. F. Crystal Shape Engineering. *Ind. Eng. Chem. Res.* **2008**, *47*, 9812−9833.

(19) Erdemir, D.; Lee, A. Y.; Myerson, A. S. Nucleation of Crystals from Solution: Classical and Two-Step Models. *Acc. Chem. Res.* **2009**, *42*, 621−629.

(20) Rodríguez-hornedo, N.; Murphy, D. Significance of Controlling Crystallization Mechanisms and Kinetics in Pharmaceutical Systems. *J. Pharm. Sci.* **1999**, *88*, 651−660.

(21) Porter, D. A.; Easterling, K. E. *Phase Transformations in Metals and Alloys*; CRC Press, 1992; Vol. 3.

(22) Zhou, Y.; Game, O. S.; Pang, S.; Padture, N. P. Microstructures of Organometal Trihalide Perovskites for Solar Cells: Their Evolution from Solutions and Characterization. *J. Phys. Chem. Lett.* **2015**, *6*, 4827−4839.

(23) Harada, M.; Katagiri, E. Mechanism of Silver Particle Formation during Photoreduction Using *in Situ* Time-Resolved Saxs Analysis. *Langmuir* **2010**, *26*, 17896−17905.

(24) Garcia, P. R. A. F.; Prymak, O.; Grasmik, V.; Pappert, K.; Wlysses, W.; Otubo, L.; Epple, M.; Oliveira, C. L. P. An *in Situ* SAXS Investigation of the Formation of Silver Nanoparticles and Bimetallic Silver-Gold Nanoparticles in Controlled Wet-Chemical Reduction Synthesis. *Nanoscale Adv.* **2020**, *2*, 225−238.

(25) Woehl, T. J.; Evans, J. E.; Arslan, I.; Ristenpart, W. D.; Browning, N. D. Direct *in Situ* Determination of the Mechanisms Controlling Nanoparticle Nucleation and Growth. *ACS Nano* **2012**, *6*, 8599−8610.

(26) Kitano, T.; Maeda, Y.; Akasaka, T. Preparation of Transparent and Conductive Thin Films of Carbon Nanotubes Using a Spreading/Coating Technique. *Carbon* **2009**, *47*, 3559−3565.

(27) Khim, D.; Han, H.; Baeg, K. J.; Kim, J.; Kwak, S. W.; Kim, D. Y.; Noh, Y. Y. Simple Bar-Coating Process for Large-Area, High-Performance Organic Field-Effect Transistors and Ambipolar Complementary Integrated Circuits. *Adv. Mater.* **2013**, *25*, 4302−4308.

(28) Gu, X.; Shaw, L.; Gu, K.; Toney, M. F.; Bao, Z. The Meniscus-Guided Deposition of Semiconducting Polymers. *Nat. Commun.* **2018**, *9*, No. 534.

(29) Deng, Y.; Zheng, X.; Bai, Y.; Wang, Q.; Zhao, J.; Huang, J. Surfactant-Controlled Ink Drying Enables High-Speed Deposition of Perovskite Films for Efficient Photovoltaic Modules. *Nat. Energy* **2018**, *3*, 560−566.

(30) Schlipf, J.; Muller-Buschbaum, P. Structure of Organometal Halide Perovskite Films as Determined with Grazing-Incidence X-Ray Scattering Methods. *Adv. Energy Mater.* **2017**, *7*, No. 1700231.

(31) Altamura, D.; Sibillano, T.; Siliqi, D.; De Caro, L.; Giannini, C. Assembled Nanostructured Architectures Studied By Grazing Incidence X-Ray Scattering. *Nanomater. Nanotechnol.* **2012**, *2*, 16.

(32) Renaud, G.; Lazzari, R.; Leroy, F. Probing Surface and Interface Morphology with Grazing Incidence Small Angle X-Ray Scattering. *Surf. Sci. Rep.* **2009**, *64*, 255−380.

(33) Li, T.; Senesi, A. J.; Lee, B. Small Angle X-Ray Scattering for Nanoparticle Research. *Chem. Rev.* **2016**, *116*, 11128−11180.

(34) Frank, C. H. Real-Time X-Ray Scattering Studies on Organic Thin Films, Mathematisch-Naturwissenschaftlichen Fakultat. Ph.D. Thesis, EberhardKarls Universitat Tubingen, 2014.

(35) Mundt, L. E.; Schelhas, L. T. Structural Evolution During Perovskite Crystal Formation and Degradation: *In Situ* and Operando X-Ray Diffraction Studies. *Adv. Energy Mater.* **2020**, No. 1903074.

(36) Barrows, A. T.; Lilliu, S.; Pearson, A. J.; Babonneau, D.; Dunbar, A. D. F.; Lidzey, D. G. Monitoring the Formation of a CH 3 NH 3 PbI 3- x Cl x Perovskite during Thermal Annealing Using X-Ray Scattering. *Adv. Funct. Mater.* **2016**, *26*, 4934−4942.

(37) Zhong, Y.; Munir, R.; Li, J.; Tang, M.-C.; Niazi, M. R.; Smilgies, D.-M.; Zhao, K.; Amassian, A. Blade-Coated Organolead Triiodide Perovskite Solar Cells with Efficiency 17%: An *In Situ* Investigation. *ACS Energy Lett.* **2018**, *3*, 1078−1085.

(38) Alhazmi, N.; Pineda, E.; Rawle, J.; Howse, J. R.; Dunbar, A. D. F. Perovskite Crystallization Dynamics during Spin-Casting: An *in Situ* Wide-Angle X-Ray Scattering Study. *ACS Appl. Energy Mater.* **2020**, *3*, 6155−6164.

(39) Masi, S.; Rizzo, A.; Munir, R.; Listorti, A.; Giuri, A.; Esposito Corcione, C.; Treat, N. D.; Gigli, G.; Amassian, A.; Stingelin, N.; Colella, S. Organic Gelators as Growth Control Agents for Stable and Reproducible Hybrid Perovskite-Based Solar Cells. *Adv. Energy Mater.* **2017**, *7*, No. 1602600.

(40) Tang, M. C.; Fan, Y.; Barrit, D.; Chang, X.; Dang, H. X.; Li, R.; Wang, K.; Smilgies, D. M.; Liu, S. F.; De Wolf, S.; Anthopoulos, T. D.; Zhao, K.; Amassian, A. Ambient Blade Coating of Mixed Cation, Mixed Halide Perovskites without Dripping: *In Situ* Investigation and Highly Efficient Solar Cells. *J. Mater. Chem. A* **2020**, *8*, 1095−1104.

(41) Liao, H.-C.; Tsao, C.-S.; Jao, M.-H.; Hsu, C.-P.; Huang, Y.-C.; Tian, K.-Y.; Shyue, J.-J.; Chen, C.-Y.; Su, C.-J.; Su, W.-F. Hierarchical I-P and I-N Porous Heterojunction in Planar Perovskite Solar Cells. *J. Mater. Chem. A.* **2015**, *3*, 10526−10535.

(42) Huang, Y.-C.; Tsao, C.-S.; Cho, Y.-J.; Chen, K.-C.; Chiang, K.-M.; Hsiao, S.-Y.; Chen, C.-W.; Su, C.-J.; Jeng, U.-S.; Lin, H.-W. Insight into Evolution, Processing and Performance of Multi- Length-Scale Structures in Planar Heterojunction Perovskite Solar Cells. *Sci. Rep.* **2015**, *5*, No. 13657.

(43) Liu, F.; Gu, Y.; Wang, C.; Zhao, W.; Chen, D.; Briseno, A. L.; Russell, T. P. Efficient Polymer Solar Cells Based on a Low Bandgap Semi-Crystalline DPP Polymer-PCBM Blends. *Adv. Mater.* **2012**, *24*, 3947−3951.

(44) Pröller, S.; Liu, F.; Zhu, C.; Wang, C.; Russell, T. P.; Hexemer, A.; Müller-Buschbaum, P.; Herzig, E. M. Following the Morphology Formation *in Situ* in Printed Active Layers for Organic Solar Cells. *Adv. Energy Mater.* **2016**, *6*, No. 1501580.

(45) Sanyal, M.; Schmidt-Hansberg, B.; Klein, M. F. G.; Colsmann, A.; Munuera, C.; Vorobiev, A.; Lemmer, U.; Schabel, W.; Dosch, H.; Barrena, E. *In Situ* X-Ray Study of Drying-Temperature Influence on the Structural Evolution of Bulk-Heterojunction Polymer–Fullerene Solar Cells Processed by Doctor-Blading. *Adv. Energy Mater.* **2011**, *1*, 363−367.

(46) Liu, F.; Ferdous, S.; Schaible, E.; Hexemer, A.; Church, M.; Ding, X.; Wang, C.; Russell, T. P. Fast Printing and *in Situ* Morphology Observation of Organic Photovoltaics Using Slot-Die Coating. *Adv. Mater.* **2015**, *27*, 886−891.

(47) Jun, Y. S.; Lee, B.; Waychunas, G. A. *In Situ* Observations of Nanoparticle Early Development Kinetics at Mineral-Water Interfaces. *Environ. Sci. Technol.* **2010**, *44*, 8182−8189.

(48) Sauter, A.; Roosen-Runge, F.; Zhang, F.; Lotze, G.; Jacobs, R. M. J.; Schreiber, F. Real-Time Observation of Nonclassical Protein Crystallization Kinetics. *J. Am. Chem. Soc.* **2015**, *137*, 1485−1491.

(49) Li, T.; Senesi, A. J.; Lee, B. Small Angle X-Ray Scattering for Nanoparticle Research. *Chem. Rev.* **2016**, *116*, 11128−11180.

(50) Treat, N. D.; Nekuda Malik, J. A.; Reid, O.; Yu, L.; Shuttle, C. G.; Rumbles, G.; Hawker, C. J.; Chabinyc, M. L.; Smith, P.; Stingelin, N. Microstructure Formation in Molecular and Polymer Semiconductors Assisted by Nucleation Agents. *Nat. Mater.* **2013**, *12*, 628−633.

(51) Davey, R. J.; Schroeder, S. L. M.; ter Horst, J. H. Nucleation of Organic Crystals-A Molecular Perspective. *Angew. Chem., Int. Ed.* **2013**, *52*, 2166−2179.

(52) Lee, H.; Kim, A.; Kwon, H.-C.; Yang, W.; Oh, Y.; Lee, D.; Moon, J. Retarding Crystallization during Facile Single Coating of NaCl-Incorporated Precursor Solution for Efficient Large-Area Uniform Perovskite Solar Cells. *ACS Appl. Mater. Interfaces* **2016**, *8*, 29419−29426.

(53) Song, X.; Wang, W.; Sun, P.; Ma, W.; Chen, Z.-K. Additive to Regulate the Perovskite Crystal Film Growth in Planar Heterojunction Solar Cells. *Appl. Phys. Lett.* **2015**, *106*, No. 33901.

(54) Lee, H.; Kim, A.; Kwon, H.-C.; Yang, W.; Oh, Y.; Lee, D.; Moon, J. Retarding Crystallization during Facile Single Coating of NaCl-Incorporated Precursor Solution for Efficient Large-Area Uniform Perovskite Solar Cells. *ACS Appl. Mater. Interfaces* **2016**, *8*, 29419−29426.

(55) Mohamad, D. K.; Freestone, B. G.; Masters, R.; Reinhardt, M.; Canning, S.; Rodenburg, C.; Lidzey, D. G. Optimized Organometal Halide Perovskite Solar Cell Fabrication through Control of Nano-particle Crystal Patterning. *J. Mater. Chem. C* **2017**, *5*, 2352−2359.

(56) Mohamad, D. K.; Griffin, J.; Bracher, C.; Barrows, A. T.; Lidzey, D. G. Spray-Cast Multilayer Organometal Perovskite Solar Cells Fabricated in Air. *Adv. Energy Mater.* **2016**, *6*, 1−7.

(57) Roe, R.-J. *Methods of X-Ray and Neutron Scattering in Polymer Science.*; Oxford University Press: New York, 2000.

(58) Fernandez-Martinez, A.; Hu, Y.; Lee, B.; Jun, Y.-S.; Waychunas, G. A. *In Situ* Determination of Interfacial Energies between Heterogeneously Nucleated CaCO3 and Quartz Substrates: Thermo-dynamics of CO2 Mineral Trapping. *Environ. Sci. Technol.* **2013**, *47*, 102−109.

(59) Chang, C.-Y.; Wang, C.-P.; Raja, R.; Wang, L.; Tsao, C.-S.; Su, W.-F. High-Efficiency Bulk Heterojunction Perovskite Solar Cell Fabricated by One-Step Solution Process Using Single Solvent: Synthesis and Characterization of Material and Film Formation Mechanism. *J. Mater. Chem. A* **2018**, *6*, 4179−4188.

(60) Yang, T.; Liu, J.; Dai, J.; Han, Y. Shaping Particles by Chemical Diffusion and Reaction. *CrystEngComm* **2017**, *19*, 72−79.

(61) Han, Y.; Yang, T.; Chen, Y. A Perspective on Morphology Controlled Synthesis of Powder by Tuning Chemical Diffusion and Reaction. *Adv. Powder Technol.* **2020**, *31*, 922−925.

(62) Woehl, T. J.; Evans, J. E.; Arslan, I.; Ristenpart, W. D.; Browning, N. D. Direct *in Situ* Determination of the Mechanisms Controlling Nanoparticle Nucleation and Growth. *ACS Nano* **2012**, *6*, 8599−8610.

(63) Moghadam, M. M.; Li, R.; Buchholz, D. B.; Li, Q.; Voorhees, P. W.; Dravid, V. P. *In Situ* Crystallization and Morphological Evolution in Multicomponent Indium Oxide Thin Films. *Cryst. Growth Des.* **2017**, *17*, 1396−1403.

(64) Hu, Q.; Zhao, L.; Wu, J.; Gao, K.; Luo, D.; Jiang, Y.; Zhang, Z.; Zhu, C.; Schaible, E.; Hexemer, A.; Wang, C.; Liu, Y.; Zhang, W.; Grätzel, M.; Liu, F.; Russell, T. P.; Zhu, R.; Gong, Q. *In Situ* Dynamic Observations of Perovskite Crystallisation and Microstructure Evolution Intermediated from [PbI6]4 Cage Nanoparticles. *Nat. Commun.* **2017**, *8*, No. 15688.

(65) Wang, B.; Young Wong, K.; Xiao, X.; Chen, T. Elucidating the Reaction Pathways in the Synthesis of Organolead Trihalide Perovskite for High-Performance Solar Cells. *Sci. Rep.* **2015**, *5*, No. 10557.

(66) Moore, D. T.; Sai, H.; Tan, K. W.; Smilgies, D. M.; Zhang, W.; Snaith, H. J.; Wiesner, U.; Estroff, L. A. Crystallization Kinetics of Organic-Inorganic Trihalide Perovskites and the Role of the Lead Anion in Crystal Growth. *J. Am. Chem. Soc.* **2015**, *137*, 2350−2358.

(67) Zeng, F. W.; Zhang, D.; Spicer, J. B. Palladium Nanoparticle Formation Processes in Fluoropolymers by Thermal Decomposition of

Organometallic Precursors. *Phys. Chem. Chem. Phys.* **2018**, *20*, 24389–24398.

(68) He, M.; Li, B.; Cui, X.; Jiang, B.; He, Y.; Chen, Y.; O'Neil, D.; Szymanski, P.; Ei-Sayed, M. A.; Huang, J.; Lin, Z. Meniscus-Assisted Solution Printing of Large-Grained Perovskite Films for High-Efficiency Solar Cells. *Nat. Commun.* **2017**, *8*, No. 16045.

(69) Stone, K. H.; Gold-Parker, A.; Pool, V. L.; Unger, E. L.; Bowring, A. R.; McGehee, M. D.; Toney, M. F.; Tassone, C. J. Transformation from Crystalline Precursor to Perovskite in PbCl2-Derived MAPbI3. *Nat. Commun.* **2018**, *9*, No. 3458.

(70) Yang, Z.; Chueh, C. C.; Zuo, F.; Kim, J. H.; Liang, P. W.; Jen, A. K. Y. High-Performance Fully Printable Perovskite Solar Cells via Blade-Coating Technique under the Ambient Condition. *Adv. Energy Mater.* **2015**, *5*, No. 1500328.

■ NOTE ADDED AFTER ASAP PUBLICATION

This paper was published after ASAP on February 02, 2021 with minor errors. The corrected version was reposted on February 05, 2021.